CHAPTER 4

Off-on detection of glutathione based on the nitrogen, sulfur codoped carbon quantum dots@MnO_2 nano-composite in human lung cancer cells and blood serum

4.1. Introduction

Now a days Glutathione (GSH) is a thiol rich tri-peptide and most predominant non-protein in the mammalian cells which is endogenously synthesized from the three amino acids L-cysteine, glycine, and L-glutamic acid. It helps in several vital functions such as detoxification, homeostasis, gene regulation, redox reactions, and metabolism [Lu (2009), Tang *et al.* (2019)]. Any change in a GSH concentration level causes various diseases such as cancer, diabetes, ageing, inflammatory, Alzheimer diseases, liver damage, cardiovascular diseases, and caducity [Li *et al.* (2014), Gupta *et al.* (2016), Ngamchuea *et al.* (2016)]. Thus, it is an urgent need to develop accurate, rapid, and sensitive detection techniques for monitoring and visualizing the change in GSH level in a clinical sample. The assignment toward the development of highly selective and sensitive detection of GSH has been extremely challenging task. Ample of sensors have been designed for the intracellular detection of GSH including electrochemistry [Lee *et al.* (2015)], high performance liquid chromatography (HPLC) [Wang *et al.* (2004)], mass spectroscopy [Tsikas *et al.* (2000)], absorbance method [Ge et al. (2019)], surface enhanced Raman spectroscopy (SERS) [Ouang et al. (2014)], and fluorescence spectroscopy [Huang *et al.* (2017)] method. Recently, fluorescence based method holds a considerable advantage over other techniques due to its high sensitivity, straightforwardness, and non-destructive properties and real time imaging [Zhang *et al.* (2014), Hu *et al.* (2014), He *et al.* (2018), Pavase *et al.* (2018)].

To date, the number of strategies counting gold nano-clusters [Tian *et al.* (2012)], organic dyes [Xu and Hepel (2011)], and semiconductor quantum dots [Liu *et al.* (2010)] have been selected as a fluorescent probe for the detection and quantification of GSH

concentrations. However, the requirement of costly chemicals, use of heavy metal in these synthesis processes, and presence of various colors and reactive species in fluorescent organic dyes, limits the potential application in biological and clinical samples. Therefore, the production of biocompatible fluorescence material is required to increase the scalability in terms of environmental and health issue.

During the past decade, the fluorescent carbon quantum dots are emerging as a fascinating class of photoluminescent nanomaterials in scientific community. These materials established a wide attention in fluorescence based sensors, energy conversion, diagnosis, catalysis, live cell imaging, optronic devices, and drug delivery with improved properties in terms of low-cost, good biocompatibility, high water solubility, strong chemical inertness, and elevated photo-stability [Lim *et al.* (2015), Li *et al.* (2012), Cao *et al.* (2007), Zhang *et al.* (2014), Zhu *et al.* (2013)]. To date, numerous synthesis process have been used for the fabrication of carbon quantum dots such as ultrasonic sound [Yang *et al.* (2015)], electrochemical oxidation [Wang *et al.* (2014)], hydrothermal treatment, acid assisted chemical oxidation [Moon *et al.* (2017)], microwave irradiation [Liu *et al.* (2015)], and laser ablation [Li *et al.* (2010)]. Nonetheless; except hydrothermal, most of these approaches suffer the use of expensive and sophisticated instrument, strong concentrated acids, and uncontrollable reaction conditions. Hydrothermal route is extensively favored as it is straightforward, green, highly efficient, and cost effective. In current, many efforts have been focused in designing nitrogen and sulfur doped carbon quantum dots for the tunable and superior emission properties [Li *et al.* (2015), Wang *et al.* (2019), Shi *et al.* (2019)]. Because of the comparable electron with drawing capacity and atomic sizes, nitrogen can form bond with carbon; whereas, sulfur delivers different emissive trap state and can responsible for

surface density state, which improves the fluorescence emission of carbon quantum dots. Thus, the production of nitrogen and sulfur doped carbon quantum dots with high fluorescence quantum yield is still interesting and challenging task.

MnO_2 nanosheet is an interesting class of transition metal dioxide with good environmental biocompatibility, low-cost, and high abundance [Kai *et al.* (2008)]. They have been authenticated as a fluorescence quencher and have attracted extensive attention in assembling the biosensor. The absorption spectrum of MnO_2 nanosheet exhibit broad range (250–600 nm) with a very intense absorption peak centered at 380 nm which enable MnO_2 nanosheets to act as a very efficient broad spectrum quencher.

Taking these advantages into account, we have assembled a MnO_2 based nano-composite with fluorescence N,S–CQDs for the 'off-on' detection of GSH. In this study, nitrogen and sulfur doped carbon quantum dots (N,S–CQDs) is produced by facile, straightforward, and low cost one-step hydrothermal treatment of tartaric acid as the carbon precursor and taurine as the nitrogen and sulfur source. As-synthesized N,S–CQDs exhibit blue color emission with comparative high quantum yield. Introduction of MnO_2 nanosheets quenches the fluorescence emission of N,S–CQDs by some strong electrostatic interaction and fluorescence resonance energy transfer process. The fluorescence can reappear after the addition of GSH into the nano-composite solution because it triggers the decomposition of MnO_2 nanosheet into Mn^{2+}, which leads to elimination of fluorescence resonance energy transfer. In addition, the developed nano-composite based material could act as an efficient nanoprobe for *in vitro* inspecting GSH in living cells and human blood serum.

4.2. Experimental Section

4.2.1. Materials and reagent

The chemicals used in the developed study were of commercial grade and ultrapure water was used as a solvent throughout the whole experiment. The salts NaCl, KCl, $CaCl_2$, $MgCl_2$, $Zn(NO_3)_2$, and $FeCl_3$ were acquired from the S D Fine-Chem Limited, India. Tryptophan (Try), Glutamic acid (Glu), Histidine (Hist), glycine (Gly), glucose (Gluc), cysteine (Cys) and taurine were procured from the Sigma-Aldrich, India. Human blood serum was gained from the Student Health Care Complex, IIT (BHU), Varanasi, India.

4.2.2. Instrumentation

Various analytical techniques have been used to characterize the sample. For the optical properties, UV-vis Absorption Spectrophotometer (Evolution 301, Thermo Scientific) and Fluorescence Spectrophotometer (Fluoromax 4, Horiba USA) have been conducted. The functional groups have been investigated by the use of Fourier Transform Infrared Spectrophotometer (FTIR, Perkin Elmer Spectrum 100). Transmission Electron Microscope (TEM, TECHNAI G^2 20 S–TWIN) was used to detect shape and size. The time resolved fluorescence decay data were obtained by the use of Edinburgh Instrument. Zeta potentials have been conducted by the use of Nano-Zetasizer (MALVERN Instruments). X-Ray Diffractometer (XRD) (Rigaku MiniFlex 600) having Cu Kα radiation source and Ni filter were used to measure the crystallinity of material in the range of 10–80° (5° per min). XPS analysis was surveyed by XPS, AMICUS, Kratos Analytical, A Shimadzu.

4.2.3. Preparation of N,S–CQDs

Nitrogen, sulfur dual doped carbon quantum dots (N,S–CQDs) were prepared by the facile one-step hydrothermal treatment of *tartaric acid* and *taurine*. Typically, tartaric acid (0.5 g) and taurine (0.2 g) were added into the 50 mL of ultrapure water in a small beaker and ultrasonicated for 10 min to dissolve the solution. Subsequently, the obtained mixed solution was transferred into a Teflon-lined stainless steel autoclave and kept at 210 ^{o}C for 5 hours. The obtained dark brown carbonaceous solution directed to the formation of N,S–CQDs. The N,S–CQDs solution was centrifuged at 12,000 rpm for 15 min to remove the larger particles and the filtrate part was purified against the 0.22 μm pore size syringe filter. The concentration of N,S–CQDs was adjusted to 40 μg/mL and kept in an incubator at 4 ^{o}C until further characterization and application.

4.2.4. Preparation of MnO_2 nanosheets

Typically, 2 mL of $KMnO_4$ solution (10 mM) was diluted with the 12 mL of ultrapure distilled water and subsequently 6 mL of glucose solution (100 mM) was added into it. The deep purple color solution of $KMnO_4$ was instantly kept for the ultra-sonication process at 35 ^{o}C up to 15 min. The dark brown colloidal solution was cooled down at room temperature. The obtained solution was centrifuged at 15,000 rpm up to 25 min and the supernatant part was discarded and resuspended in water. This process was repeated 3–4 times to sanitize the MnO_2 nanosheets. The concentration of MnO_2 nanosheets was adjusted to 200 μg/mL and the obtained sample was kept in 4 mL of distilled water in an incubator at 4 ^{o}C until further apply.

4.2.5. Preparation of N,S–CQD–MnO_2 nano-composite

Typically, 50 μL of the MnO_2 nanosheet solution with different concentration were dispersed into the 50 μL of N,S–CQDs (40 μg/mL) and final volume was adjusted to 1 mL by using phosphate buffer (10 mM, pH 7.4). After 5 min of ultrasonication, the quenching properties of the reaction system were traced by the fluorescence detection system at λ_{cx}=360 nm.

4.2.6. Detection of glutathione

For the selectivity experiment, the solution of different interfering agents (100 μM) was prepared in ultrapure water. The 100 μL of these interfering ingredients were mixed with the aforementioned nano-composites (70 μg/mL), which were maintained to 1 mL with phosphate buffer (10 mM, pH 7.4). For the sensitivity, different GSH concentrations (0–100 μM) were prepared by simple dilution techniques. The inspection was carried out by the addition of 100μL different GSH concentrations into composite based nanoprobe (70 μg/mL) and parallel emission spectra were scanned at λ_{ex}=360 nm after 6 min of incubation. The detection limit was measured by the equation 3σ/m along with S/N=3 from the stern-Volmer plot between $(F-F_0)/F_0$ and GSH concentration.

4.2.7. MTT assay

The cell viability assay of N,S–CQD–MnO_2 was performed by using 3-(4,5-dimethyl thiazol-2yl)- 2,5-diphenyl tetrazolium bromide (MTT) as a standard protocol by using A549 human lung cancer cell line. TheA549 cells were preserved in the Dulbecco's Modified Eagle Medium, supplemented (Gibco) with the 10% fetal bovine serum at 37 °C in 5% CO_2 in a humidified atmosphere. The A549 cells were grown in 96-well plate (1.0×10^4 cells per well) and allowed to stick overnight at 37 °C. Then, the medium was removed and the cells

were incubated with the 50 μL of different N,S–CQD–MnO_2 concentration (20, 40, 60, 80, 100, and 200 μg/mL) for 24 hours. The medium was then removed and 250 μL of DMSO was added to dissolve the formazan crystals. Subsequently, the absorbance spectra were traced at 570 nm in a micro-plate reader. The cytotoxicity and viability were calculated by the formula given in the previous chapter (**equation 2.1** and **2.2**) in a **section 2.5.1**.

4.2.8. *In vitro* cellular imaging

Lung cancer cells (A549) were seeded in tissue culture plates ($1x10^4$ cells per well) and incubated for 24 hours at 37 ^oC in CO_2 atmosphere. Then, the exhausted media was rejected and cells were washed with the PBS buffer (10 mM at pH 7.4). Subsequently, the cells were treated with the 400 μL fresh Dulbecco's Modified Eagle Medium, supplemented (Gibco) containing 70 μg/mL nanoprobe solution. After incubating overnight for 12 hours, the A549 cells were further washed with the PBS and monitored for the *in vitro* fluorescence cellular imaging by using inverted fluorescence microscope.

4.3. Results and Discussion

4.3.1. Characterization of N,S–CQDs, MnO_2 nanosheet, and N,S–CQD–MnO_2 nanocomposite

The N,S–CQDs were produced from the tartaric acid and taurine precursors, as mentioned above (**Scheme 4.1**).

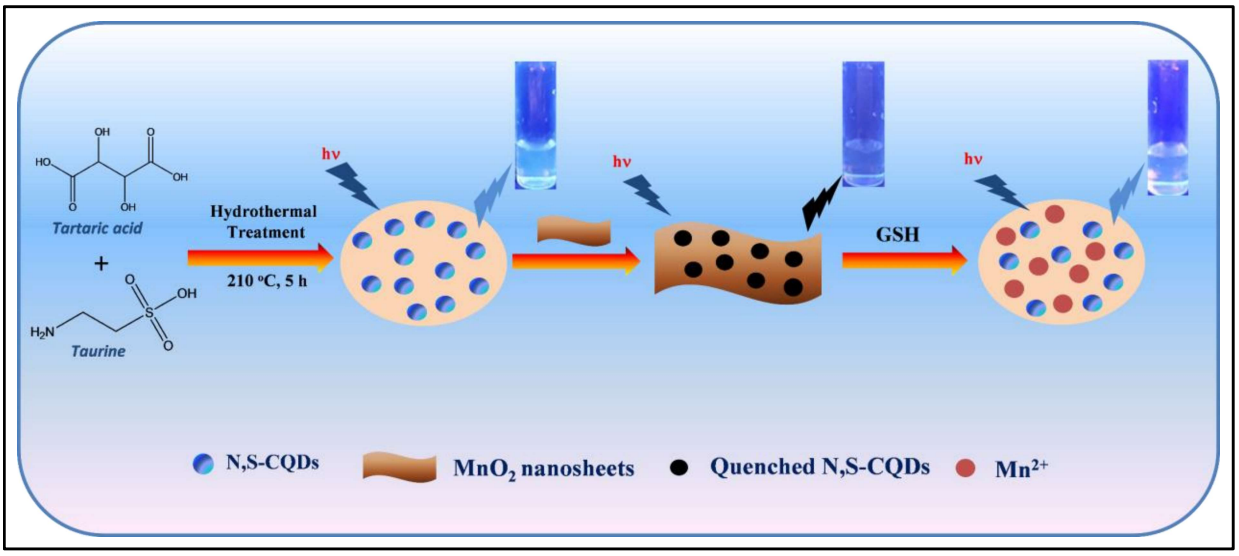

Scheme 4.1 Schematic representation of designed N,S–CQD–MnO_2 based nanoprobe for the 'off-on' detection of GSH.

The TEM observation confirmed the formation of nearly spherical N,S–CQDs along with the diameter ranges from 2 to 3 nm (**Figure 4.1a**). As presented in **Figure 4.1b**, the broad XRD peak at 25° along with (002) reflection confirmed the amorphous nature of N,S–CQDs [Baker *et al.* (2010)]. This outcome is consistent with the result attained from the broad ring in selected area electron diffraction SAED micrograph (**Figure 4.1c).** The FTIR spectrum of N,S–CQDs (**Figure 4.1d)** reveals the peak at 590 cm^{-1}, 1105 cm^{-1}, 1250 cm^{-1}, 2860 cm^{-1}, 2919 cm^{-1}, and 3421 cm^{-1} advocated the occurrence of C–S, C–O, C–N, –C–H, =C–H, and –OH/–NH stretching or bending vibrations. The characteristic peaks at 1641 cm^{-1}, and 1445 cm^{-1} are due to the HN–C=O and aromatic ring C=C–C, respectively; this result established that as-prepared nanomaterial possesses some graphene like structure [Coates *et al.* (2006)].

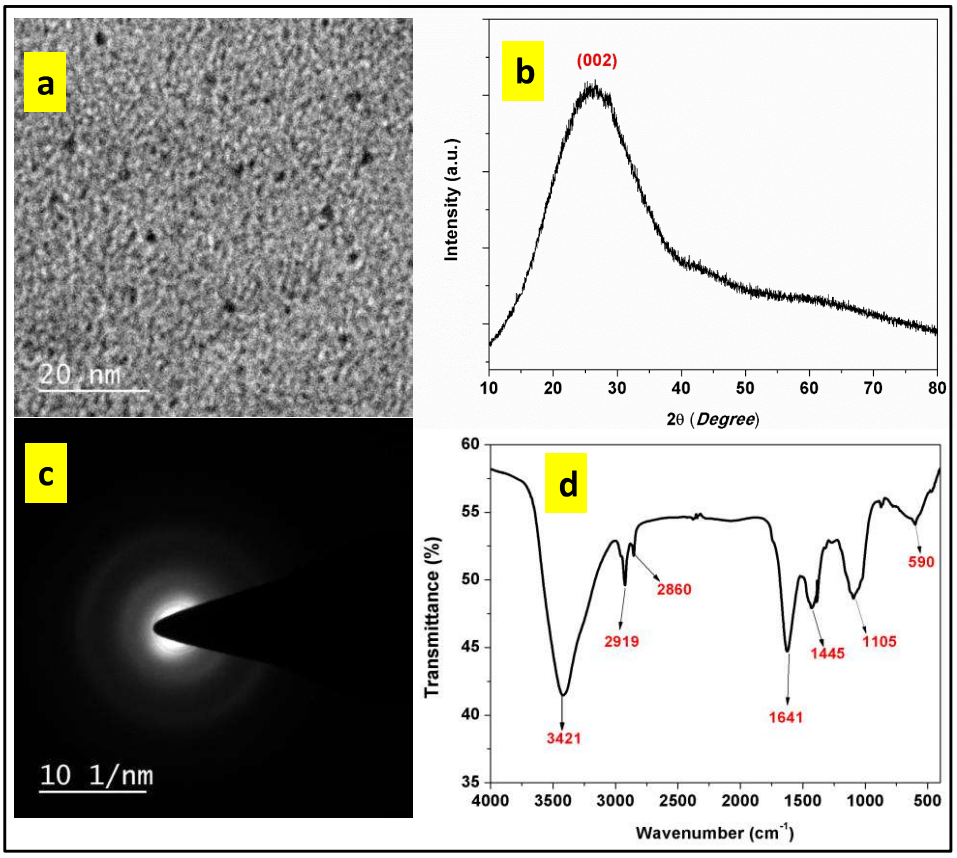

Figure 4.1 (a, c) TEM and SAED micrograph, (b, d) XRD and FTIR spectrum of the as-synthesized N,S–CQDs.

The X-Ray photoelectron spectroscopy (XPS) studies surveyed the composition and bonding present in the synthesized nanomaterial. The XPS full shot spectrum of N,S–CQDs consist four peaks, which are accountable for the S 2p (164 eV), C 1s (286 eV), N 1s (401 eV), and O 1s (533 eV), as shown in **Figure 4.2**. Therefore, this outcome revealed that the synthesized nanomaterials are efficiently doped with nitrogen and sulfur. The C 1s spectrum established the presence of C–C/C=C at 284.2 eV, C–S at 285.2 eV, C–OH/C–N at 286.1 eV, and C=O at 287.2 eV (**Figure 4.3a**). The S 2p spectrum deconvoluted into three peaks at

163.6 eV, 164.5 eV, and 165.6 eV, which are responsible for the C–S–H, C–S–C, and S=O, respectively (**Figure 4.3b**) [Li *et al.* (2014), Chaudhari *et al.* (2014)]. The N 1s spectrum advocated the peak of C–N–C, N–C_3, and N–H at 400.1 eV, 401.0 eV, and 401.9 eV, respectively (**Figure 4.3c**) [Bano *et al.* (2018)]. The O 1s spectrum exhibit binding energies located at 531.9 eV and 533.1 eV, which are advocated to the occurrence of C–O–C/C–OH and C=O, respectively (**Figure 4.3d**) [Zhang *et al.* (2012)]. Therefore, XPS studies consistent with the result obtained from the above FTIR analysis, which elaborated the structural analysis of N,S–CQDs.

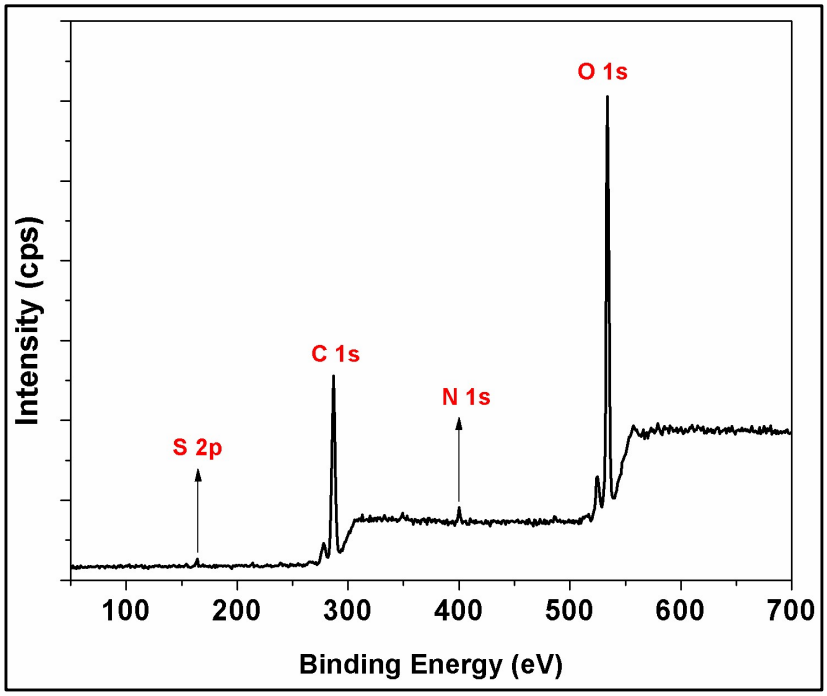

Figure 4.2 XPS full survey of as-synthesized N,S–CQDs.

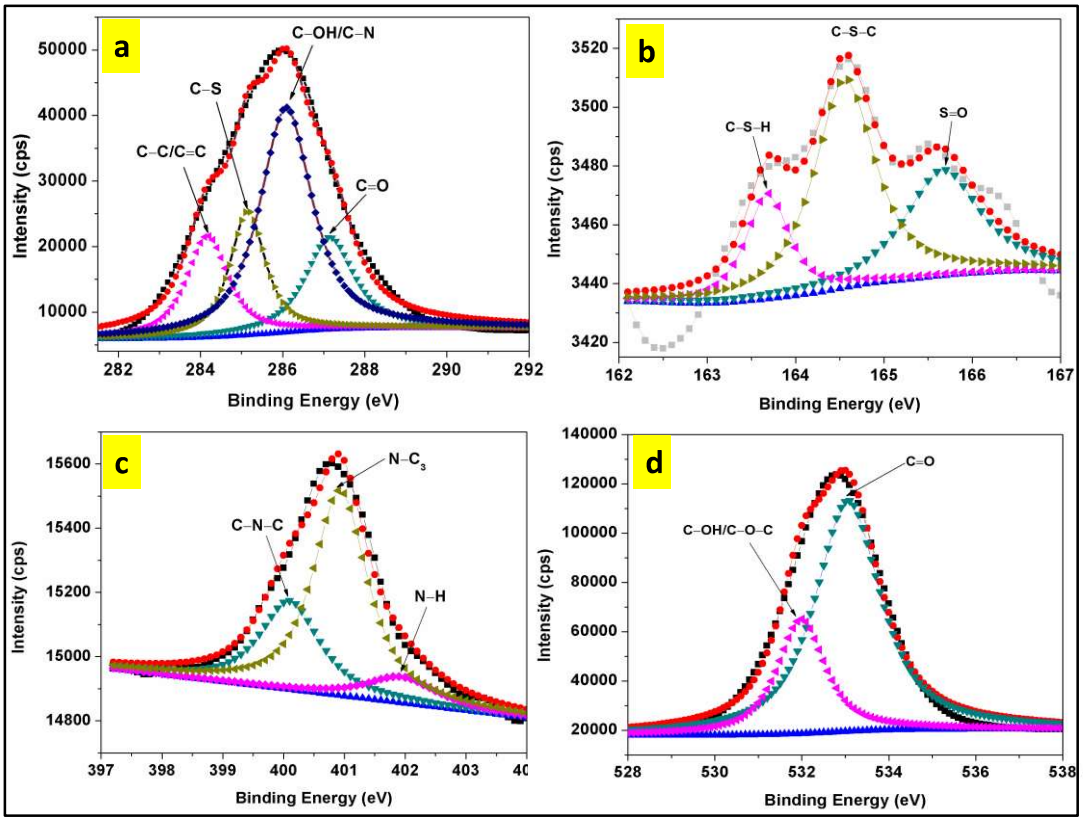

Figure 4.3 Deconvoluted XPS spectra (a) C 1s, (b) S 2p, (c) N 1s, and (d) O 1s spectra of as-syntheized N,S–CQDs.

The aqueous solution of as-fabricated N,S–CQDs displayed the two UV-vis absorption peak at 256 nm and 365 nm, which caused to the π–π* of C=C and n–π* of C=O/C=N/C=S transition, respectively (**Figure 4.4a**) [Bano *et al.* (2018), Zhang *et al.* (2012), Mei *et al.* (2016)]. Additionally, the N,S–CQDs demonstrated the excitation-dependent tuned emission between 240 nm and 400 nm excitation range and maximum emission has observed at 360 nm, as shown in **Figure 4.4b.** Meanwhile, the N,S–CQDs exhibits strong blue color photoluminescence under the UV-lamp of 365 nm, as shown in

inset **Figure 4.4b**. As given in **Figure 4.4c**, the blue color fluorescence of N,S–CQDs is supported by the Commission International De L'Eclairage index (CIE) at (0.17, 0.17), which is gained from the emission spectrum at 360 nm excitation. The strong fluorescence of N,S–CQDs should be accredited to the radiative recombination of electrons and holes trapped on the N,S–CQDs surface due to the presence of sulfur and nitrogen [Dong et al. (2013), Bao *et al.* (2011)]. In addition, the synthesized N,S–CQDs possesses comparatively high quantum yield (QY) up to 47.4 % in reference to the quinine sulfate [Li *et al.* (2015), Lin & Zhang (2012), Zhou *et al.* (2017), Kaur *et al.* (2019), Dong *et al.* (2012)]. Additionally, the fluorescence stability of as-synthesized N,S–CQDs is checked in a high ionic strength solution (**Figure 4.4d**).The insignificant effect was observed after the addition of NaCl concentration (0–10 M) confirmed that the N,S–CQDs are non-ionizable and highly stable in the high ionic strength condition. Furthermore, after keeping N,S–CQDs for 12 months at 4 ^{o}C, almost no obvious change in fluorescence emission was detected, as shown in **Figure 4.5a**. The pH factor on the emission of N,S–CQDs was also deliberated carefully, as represented in **Figure 4.5b**. On increasing pH from 2 to 8, a very small change was occurred in a fluorescence emission and up to this pH, it decreased gradually. The fluorescence quenching in an extremely basic condition ascribed to the different deprotonation degree of surface moieties present in the N,S–CQDs. Therefore, the wide pH range from 2 to 8 could be used for further application. Thus, the above-mentioned result supports that the synthesized N,S–CQDs could be proficiently used as a fluorescent material for the several analytical purpose.

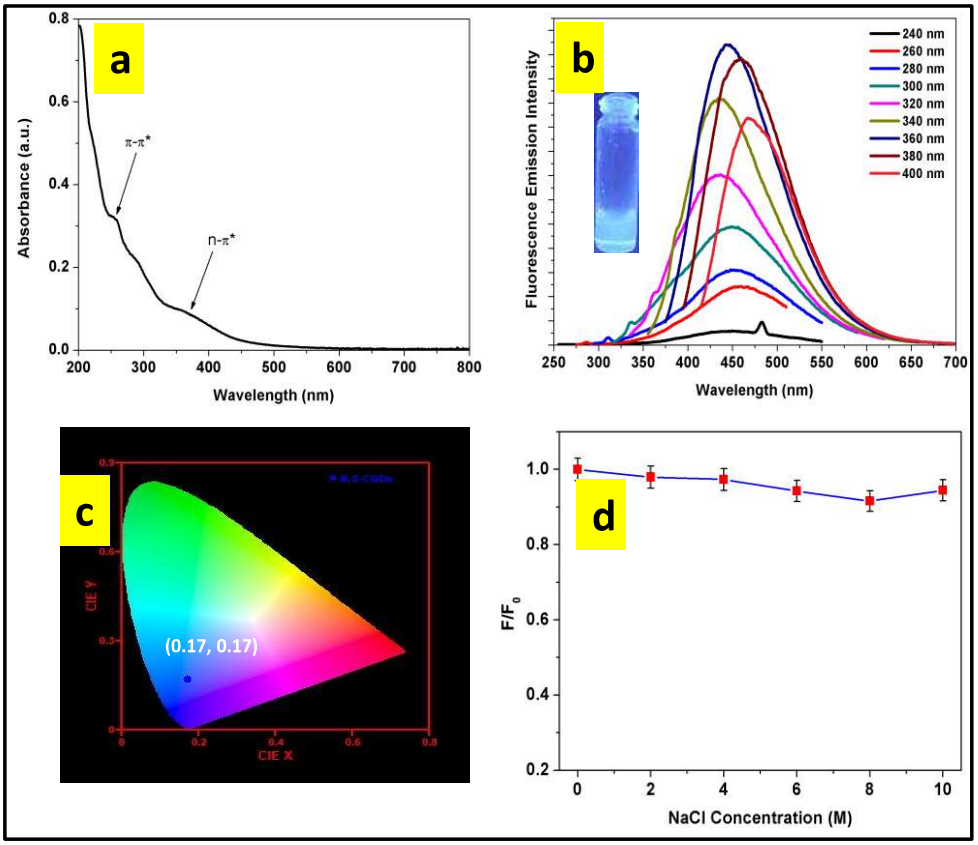

Figure 4.4 (a) UV-vis absorption spectrum of N,S–CQDs, (b) excitation dependent fluorescence emission spectra of N,S–CQDs after the excitation of 240, 260, 280, 300, 320, 340, 360, 380, and 400 nm), whereas inset shows the blue emission of N,S–CQDs at λ_{ex}=365 nm, (c) CIE co-ordinates obtained from the emission spectrum at 360 nm excitation, (d) fluorescence stability under the high NaCl strength (0–10 M).

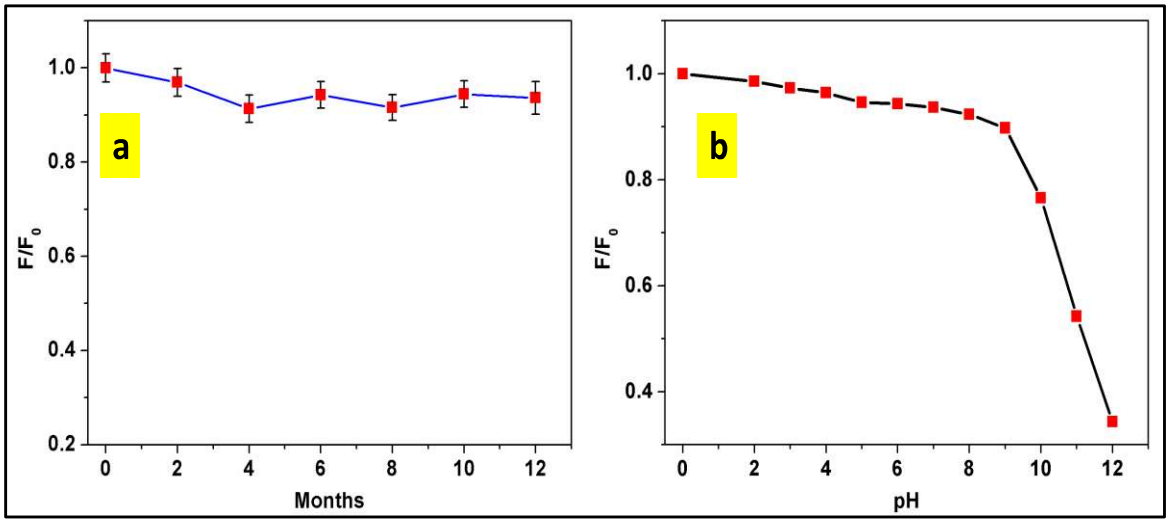

Figure 4.5 (a) Month wise fluorescence stability of N,S–CQDs, (b) effect of pH on the fluorescence emission intensity.

The MnO_2 nanosheet is prepared by the afore-mentioned method. As shown in **Figure 4.6a**, the UV-vis absorption spectrum of MnO_2 nanosheets displayed the broad absorption peak at 380 nm; this result reveals the successful formation of MnO_2 nanosheets. In the FTIR spectrum of MnO_2 nanosheet, the appearance of a peak located at 476 cm^{-1} is because of Mn–O stretching vibration (**Figure 4.6b)**.

The full scan XPS survey spectrum of N,S–CQD–MnO_2 established the existence of C, O, N, S, and Mn element, which exploring the fusion of Mn into the N,S–CQDs framework **(Figure 4.7)**. As given in **Figure 4.8a**, the splitting between Mn $2p_{3/2}$ (642.3 eV) and $2p_{1/2}$ (653.9 eV) was found to be 11.6 eV, establishing the presence of MnO_2 [Xu *et al.* (2014)]. In the O 1s spectrum of N,S–CQD–MnO_2 nano-system **(Figure 4.8b)**, the appearance of extra peak at 529 eV (Mn–O) and peak shift from 531.9 eV to 532.6 eV

(C–OH/C–O–C) and 533.1 eV to 533.5 eV (C=O), revealing the incorporation of MnO_2 nanosheets into the N,S–CQDs [Xu *et al.* (2017)].

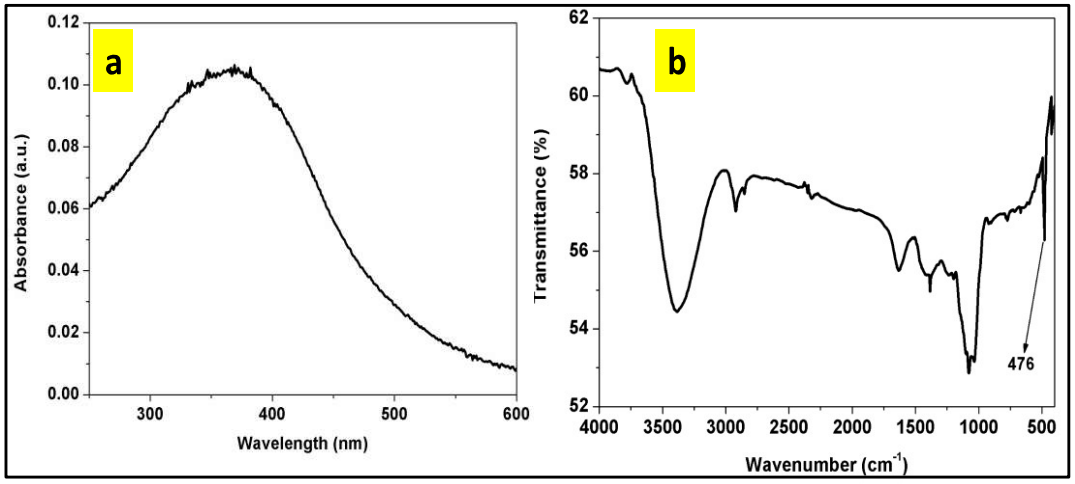

Figure 4.6 (a) UV-vis absorption spectrum of MnO_2 nanosheets, (b) FTIR spectra of MnO_2 nanosheets.

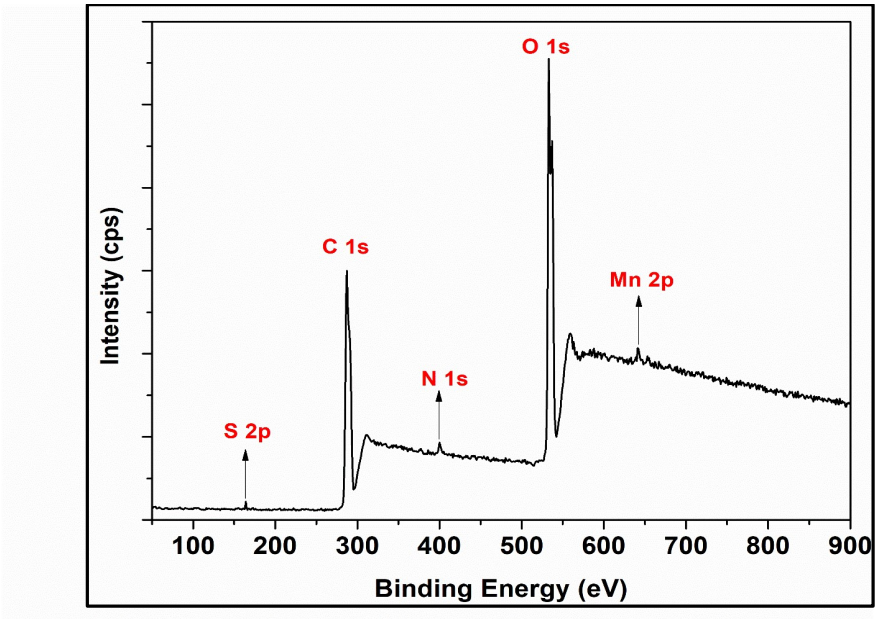

Figure 4.7 Wide scan XPS spectrum of N,S-CQDs–MnO_2 nanosheets.

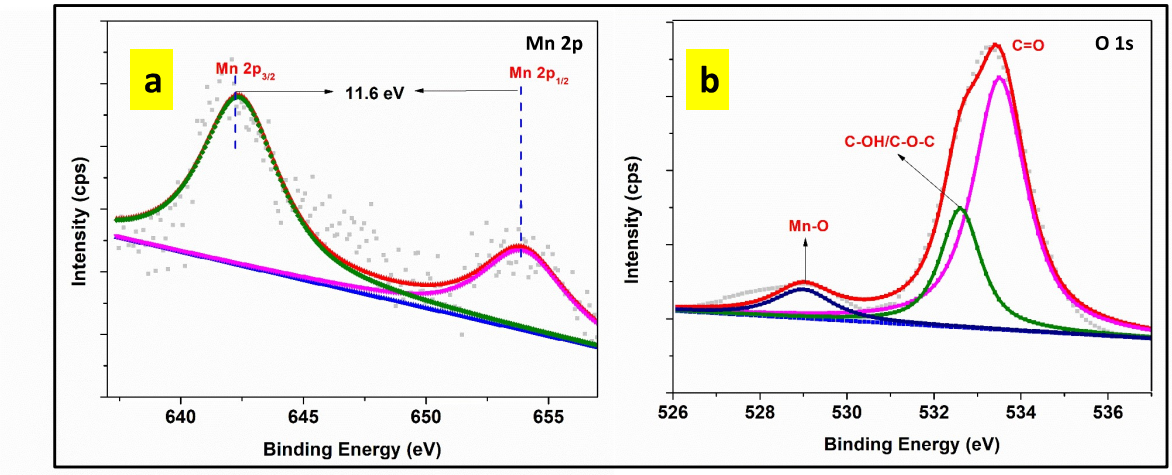

Figure 4.8 (a) Mn 2p spectrum, (b) O 1s spectrum of N,S-CQDs–MnO_2 nanosheets.

Moreover, the acquirement of the N,S–CQD–MnO_2 composite is probed into the TEM micro-images, established that the as-prepared N,S–CQDs were well decorated on the surface of MnO_2 nanosheets (**Figure 4.9a & 4.9b**). Further, the fluorescence emission of N,S–CQDs decreased with the increased MnO_2 concentration from 0 to 100 µg/mL and turn out to be more deeper as the concentration increased (**Figure 4.9c** and inset **Figure 4.9c**). In a same set of experiment, it was also found that maximum quenching efficiency has measured up to 88.9 % at 70 µg/mL concentration of MnO_2, as given in **Figure 4.9d**. Thus, 70 µg/mL of MnO_2 nanosheets was chosen as an optimum concentration for turn off fluorescence emission of N,S–CQDs.

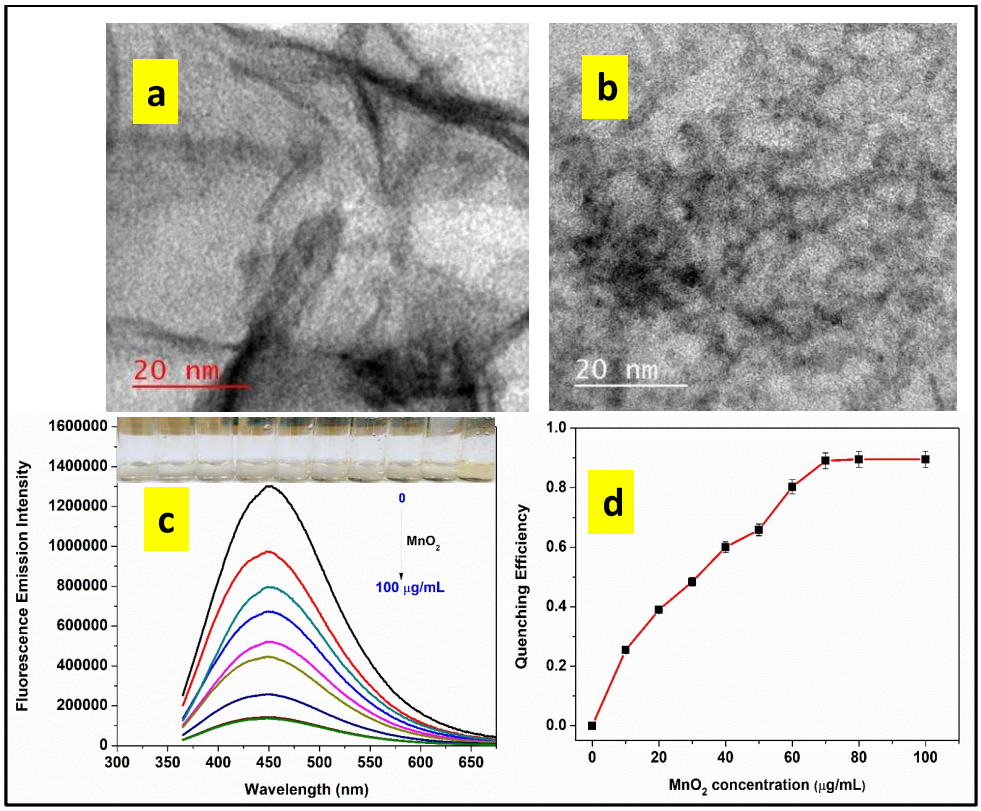

Figure 4.9 (a, b) TEM micro-image of MnO_2 nanosheets and N,S–CQD–MnO_2 nano-composites, (c) fluorescence emission spectra of N,S–CQDs as a function of different MnO_2 concentrations (0–100 μg/mL), while inset shows the corresponding color change, and (d) the graph between the concentration of MnO_2 nano-sheets and $(F_0–F)/F_0$ (quenching efficiency); where F_0 and F is the fluorescence emission of N,S–CQDs before and after addition of MnO_2 nanosheets.

The fluorescence turn off mechanism by the use of MnO_2 nanosheets was also studied carefully. As demonstrated in **Figure 4.10a**, the UV-vis absorption spectrum of MnO_2 nanosheets overlaps with the excitation (360 nm) and emission (450 nm) of synthesized N,S–CQDs, this result supports the occurrence of inner filter effect. Further, from the di-exponential fluorescence lifetime decay of N,S–CQDs, it is found that lifetime reduces to 3.14 ns from 5.55 ns in presence of MnO_2 nanosheets (**Figure 4.10b, Table 4.1**). The

decrease in lifetime confirmed the fluorescence resonance energy transfer from the synthesized N,S–CQDs donor to MnO_2 acceptor. It is given in the literature that the inner filter effect accompanied by the change in fluorescence lifetime leads to the possibility of fluorescence resonance energy transfer [Blagoi (2004)]. Thus, the preponderant quenching was related to the fluorescence resonance energy transfer from fluorescence N,S–CQDs donor to MnO_2 acceptor. The zeta potential of the N,S–CQDs in the presence of MnO_2 nanosheet altered from –4.51 to +0.08 mV, as shown in **Figure 4.11**. This result indicating that MnO_2 nanosheet absorbed the synthesized N,S–CQDs *via* strong electrostatic interaction. Therefore, fluorescence quenching could be related to the fluorescence resonance energy transfer and strong electrostatic interaction between N,S–CQDs and MnO_2 nanosheet.

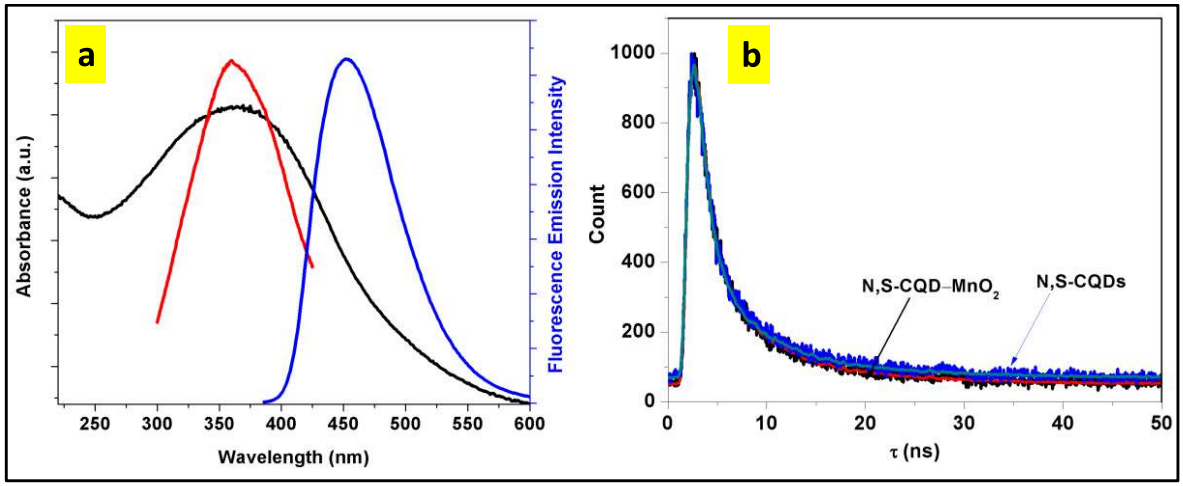

Figure 4.10 (a) The black line displays the UV-vis absorption spectrum, while red and blue indicates the excitation and emission spectrum of N,S–CQDs, respectively, (b) time resolve fluorescence decay curve of N,S–CQDs with or without MnO_2 nano-sheets.

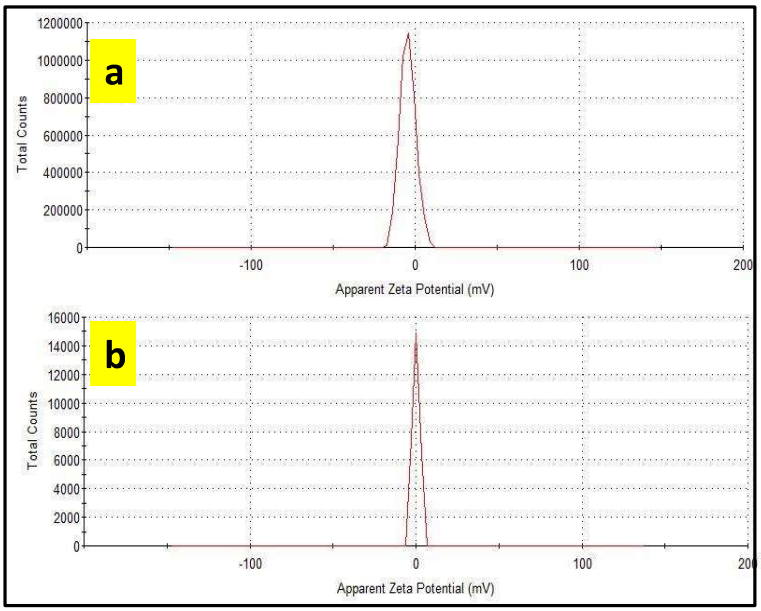

Figure 4.11 (a, b) Zeta-potential of N,S–CQDs with or without MnO_2 nanosheets.

Table 4.1 Di exponential lifetime fitting data of N,S–CQDs and N,S–CQD–MnO_2 nanohybrid.

Sample	Lifetime (ns)	Weight (%)	Chi-square (χ^2)	Average lifetime (ns)
N,S–CQDs	τ_1=0.16 τ_2=5.58	15.21 84.79	1.121	5.55
N,S–CQD–MnO_2	τ_1=0.08 τ_2=3.17	30.69 69.30	1.170	3.14

4.3.2. Detection assay

Additionally, GSH can lead to the destruction of MnO_2 sheet by some redox processes. In this process, MnO_2 reduces itself into Mn^{2+} and in the meantime, GSH itself oxidizes to GSH di-sulfide (GS-SG), as displayed in **equation 4.1** [Deng *et al.* (2011)]. Thus, our synthesized nano-composite could possibly perform as a nanoprobe for GSH detection.

$$GSH + MnO_2 + HSG + 2H^+ \rightarrow GS - SG + Mn^{2+} \qquad 4.1$$

Kinetic of the proposed sensing system toward GSH detection is also deliberated carefully as a function of time in the presence of 100 μM GSH concentrations. As shown in **Figure 4.12**, it was found that the fluorescence of the detection system after the addition of GSH (100 μL) increased gradually with the increased time up to 6 min and then remains constant. Consequently, 6 min is considered as optimum time for further detection process.

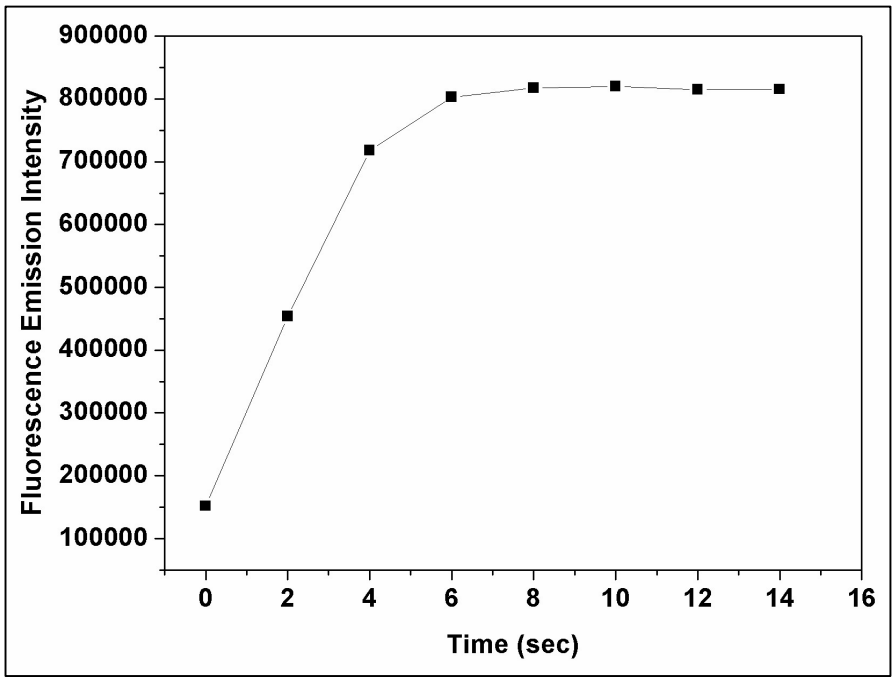

Figure 4.12 Kinetics study of the fluorescence reappearance of the N,S–CQD–MnO_2 probe in the presence of 100 μM GSH.

Inherent cytotoxicity of the prepared N,S–CQD–MnO_2 is also a significant factor to be considered into an account in designing the above-mentioned fluorescence nanoprobe. To check the cytotoxicity, the MTT assay of the N,S–CQD–MnO_2 with different concentrations

was assessed by computing the cell viability. The A549 cells were incubated with the nanoprobe of concentration (20, 40, 60, 80, 100, and 200 μg/mL) for 24 hours. The measured cell viabilities were above the 84 % when the concentrations of the nanoprobe lower than the 100 μg/mL (**Figure 4.13a)**. This outcome established that our synthesized composite based nanoprobe possessed low cytotoxicity and excellent biocompatibility; thus, it can be used as a probe in determination and inspection of GSH. As demonstrated in **Figure 4.13b**, with the increased GSH concentration from 0 to 100 μM, the fluorescence emission intensity of N,S–CQDs increased gradually and quenched N,S–CQDs got 'turn on' (inset **Figure 4.13b**). Noticeably, a good linear correlation graph is obtained in the GSH concentration range from 0.1 to 0.7 μM along with R^2=0.994 and linear equation $(F–F_0)/F_0$=1.77[GSH]+0.089, as represented in **Figure 4.13c**. In the same experiment, the detection limit was found to be 0.012 μM. It is also found that our synthesized composite based nanoprobe is superior to another earlier reported fluorescence and absorbance method, as given in **Table 4.2** [Zhang *et al.* (2014), Han *et al.* (2009), Ma *et al.* (2012), Shamsipur *et al*. (2014), Feng *et al.* (2017), Di *et al.* (2017), Cai *et al.* (2014), Yan *et al.* (2016), Ju *et al.* (2016), Chen *et al.* (2012)]. To enhance the sensing performance of our synthesized nanoprobe, the selectivity experiment was performed in different amino acids (glutamic acid, cysteine, glycine, tryptophan, and histidine) along with some other biomolecules and metal interference (ascorbic acid, uric acid, glucose, Na^+, K^+, Ca^{2+}, Mg^{2+}, Zn^{2+}, and Fe^{3+}). **Figure 4.13d** shows the selectivity experiment, which revealed that the N,S–CQD–MnO_2 nano-composite exhibit remarkable change in fluorescence emission on adding GSH (100 μM). Although, cysteine (Cys) and ascorbic acid (AA) also caused fluorescence change upto some extent along with same concentrations. Though, it is found that concentration of GSH (mM levels) is higher to that

of Cys and AA (μM levels) in living or biological systems [Zhu *et al.* (2019)]. Thus, our designated N,S–CQD–MnO_2 nano-composite based probe is specific for the GSH detection.

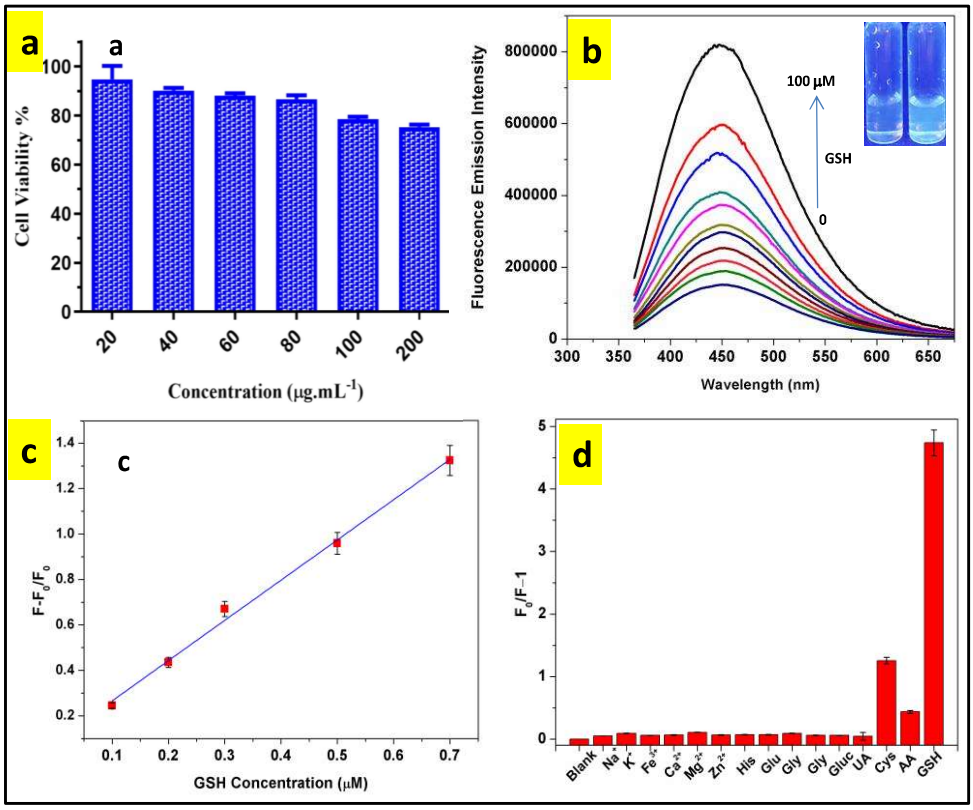

Figure 4.13 (a) Graph of cell viability assay of N,S–CQD–MnO_2 nano-composite in A549 cells, (b) emission spectra of N,S–CQDs in association with GSH concentration from 0 to 100 μM, inset illustrates the fluorescence image at λ_{ex}=365 nm, (c) parallel linear calibration graph between $(F-F_0)/F_0$ GSH concentrations from 0.1 to 0.7 μM; where F_0 and F are fluorescence emission of N,S–CQDs before and after incubation of GSH into the N,S–CQD–MnO_2 nanocomposite, and (d) selectivity of the proposed sensing system in presence of amino acids along with some other biomolecules and metal interfering agent.

Table 4.2. Comparative study of synthesized N,S–CQD–MnO_2 composite based nanoprobe with earlier reported method.

Method	Materials	Linear range (μM)	Detection limit (μM)	Ref.
Fluorimetry	g–C_3N_4–MnO_2	0–2000	0.2	[Zhang *et al.* (2014)]
Fluorimetry	CdTe–QDs–Hg^{2+}	0.6–20	0.1	[Han *et al*. (2009)]
Colorimetric	Fe_3O_4 nanoparticles	3–30	3	[Ma *et al.* (2012)]
Colorimetric	Carbon nanodots	0–7	0.3	[Shamsipur *et al.* (2014)]
Colorimetric	Gold nanoclusters	2–25	0.42	[Feng et al. (2017)]
Colorimetric	MnO_2 sheet	10–100	0.5	[Di *et al.* (2017)]
Absorbance	AuNPs	0.04–0.28	0.01	[Chen *et al*. (2012)]
Fluorimetry	C-Dots–MnO_2 sheet	1–10	0.3	[Cai *et al.* (2015)]
Absorbance	Ag NPs-TMB	0.1–160	0.013	[Ju *et al.* (2016)]
Fluorimetry	GQDs–MnO_2 sheet	0.5–10	0.15	[Yan *et al.* (2016)]
Fluorimetry	N,S–CQD–MnO_2	0.1–0.7	0.012	[Bano et al. (2020)]

4.4. Real sample analysis

To demonstrate the reliability and feasibility, the as-synthesized composite based nanoprobe was applied for *in vitro* detecting and imaging GSH in A549 human lung cancer cell. The cancerous cells were incubated with the composite based nanoprobe (70 $\mu g\,mL^{-1}$) at 37 °C for 12 hours. As illustrated in **Figure 4.14a**, no apparent fluorescence was detected for the imaging of A549 cells. As presented in **Figure 4.14b,** when the A549 cells were incubated with the composite based nanoprobe, noticeable fluorescence was observed in a blue channel. **Figure 4.14c** exhibits the corresponding fluorescence response of A549 cells in a red region. Thus, this result indicating that intracellular GSH reacted with our synthesized N,S–CQD–MnO_2 nanocomposite, which supporting the aforementioned fluorescence analysis. As displayed in **Figure 4.14d**, the bright-field micrograph established that the A549 cells were still alive and can preserve their normal morphology during the imaging tests.

Accordingly, our synthesized nanoprobe could effortlessly detect and image GSH in cancerous cells.

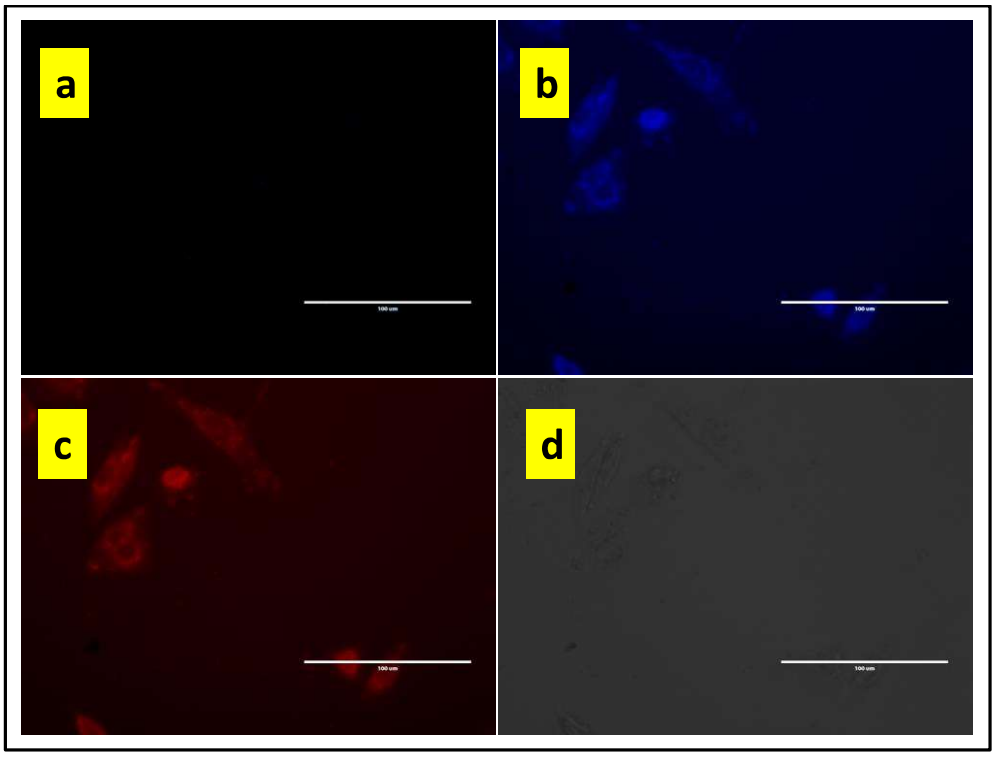

Figure 4.14 *In vitro* cell imaging of GSH in A549 human lung cancer cells (a) Intracellular fluorescence microscopic image of A549 cells, (b and c) A549 cells incubated with N,S–CQD–MnO_2 nanocomposite in a blue and red region, (d) corresponding bright-field image; the scale bars are 100 µm.

The practicability of the as-developed sensing method was further investigated in human blood serum. The collected blood serum sample was centrifuged at the rate of 12,000 rpm and the supernatant (pale yellow part) was taken. The sample was diluted 50 times with ultrapure water and spiked through the different GSH concentration (5 µM, 10 µM, and 15 µM). The sample was investigated with the proposed method. Without spiking, the GSH concentration in serum sample was measured to be 0.63 µM. After spiking, the found GSH

were 5.56 μM, 10.40 μM, and 15.74 μM. The calculated GSH recoveries were in the range of 97.7–100.7 %. The corresponding relative standard deviations (RSD) were less than 4 %, as represented in **Table 4.3**. Therefore, our synthesized N,S–CQD–MnO_2 based nanoprobe is feasible and reliable to identify the GSH in cancerous cells and blood serum sample.

Table 4.3. GSH detection in a human blood serum and RSD for the three independent measurements.

blood serum	found GSH (μM)	spiked GSH (μM)	found GSH (μM)	recovery (%)	RSD (%)
Serum 1	0.63	5	5.56	98.6	2.56
		10	10.40	97.7	3.03
		15	15.74	100.7	2.94

4.5. Conclusion

In conclusion, a synthetic approach was developed for the off-on sensing of GSH by using N,S–CQD–MnO_2 nano-composite based nanoprobe. Based on the fluorescence recovery by GSH, the synthesized nanoprobe possesses high sensitivity with multi interesting features including easy preparation, economic, and less cytotoxicity. Apart from this, the present sensing system is successfully demonstrated good feasibility for *in vitro* imaging GSH in A549 human lung cancer cell. Further, the practicability of the proposed sensing system is also efficaciously applied to human blood serum in quantification of GSH. Such a highly sensitive nanoprobe could be potentially established as a disease diagnostic and various other analytical applications in the future.